Redox control of particle deposition from drying drops

Pauline Galy, Tiffany Guitton-Spassky, Catherine Sella, Laurent Thouin, Maxime Vitale, Damien Baigl

Redox control of particle deposition from drying drops

*Pauline E. Galy,[1] Tiffany Guitton-Spassky,[1] Catherine Sella,[1] Laurent Thouin,[1] Maxime R. Vitale,[2] and Damien Baigl[1,]**

[1]PASTEUR, Department of Chemistry, École Normale Supérieure, PSL University, Sorbonne Université, CNRS, 75005 Paris, France.

[2]UMR 7203, Department of Chemistry, Ecole Normale Supérieure, PSL University, Sorbonne Université, CNRS, 75005 Paris, France

Keywords: Coffee-ring effect; colloids; ferrocene; redox-sensitive; surfactants; evaporation; Particle patterning

Abstract

The coffee-ring effect (CRE), which denotes the accumulation of non-volatile compounds at the periphery of a pinned sessile drying drop, is a universal and ubiquitous yet complex phenomenon. It is crucial to better understand and control it, either to avoid its various deleterious consequences in many processes requiring homogenous deposition or to exploit it for applications ranging from controlled particle patterning to low-cost diagnostics. Here, we report for the first time the use of a reduction-oxidation (redox) stimulus to cancel the

CRE or harness it, leading to a robust and tunable control of particle deposition in drying sessile drops. This is achieved by implementing redox-sensitive ferrocenyl cationic surfactants of different chain lengths in drying drops containing anionic colloids. Varying surfactant hydrophobicity, concentration and redox state allows us not only to control the overall distribution of deposited particles, including the possibility to fully cancel the CRE, but also to modify the microscopic organization of particles inside the deposit. Notably, all other parameters being fixed, this method allows the adjustment of the deposited particle patterns, from polycrystalline rings to uniform disks, as a function of the oxidation rate. We show that the redox control can be achieved either chemically by addition of oxidants, or electrochemically by applying a potential for additive-free and reversible actuation in a closed system. This correlation between the redox state and the particle pattern opens perspective for both redox-programmable particle patterning and original diagnostic applications based on the visual determination of a redox state. It also contributes to clarify the role of surfactant charge and its amphiphilic character in directing particle deposition from drying suspensions.

Introduction

When a drop of a suspension of non-volatile compounds is deposited on a solid surface, its evaporation leads to a ring-shaped deposit. This ubiquitous phenomenon, which occurs when the contact line is pinned on the substrate, is called the coffee-ring effect (CRE).[1] It occurs not only with practically any type of liquid containing non- volatile solutes like colloids, nanoparticles, or proteins, but also with insoluble particle-laden liquids dissolving in another partially miscible liquid phase (liquid-liquid CRE).[2] This has led to a rich literature devoted to this phenomenon, which remains however not fully understood nor predictable because of its multi-scale, multi-component and unsteady characters.[3,4] As many technical processes are relying on deposition of homogeneous layers of material during a solution evaporation, CRE

appears as a serious obstacle for a plethora of applications with deleterious impacts in industrial fields ranging from inkjet printing[5] to biotechnologies.[6–8] Conversely, it can be seen as a tool[9] to organize particles on surfaces[10–13] or an innovative solution for low-cost diagnostic applications.[14–18] There is thus a general quest for methods to understand, cancel and/or control this phenomenon. Perturbing evaporation or contact line pinning using external triggers was shown to be efficient[19–21] but is not easily implementable. In contrast, formulation approaches by using proper additives, such as polymers or binary mixtures,[22,23] offer easy solutions but can perturb the system at high concentration and usually lack external addressability. Among additives, surfactants are thus particularly interesting candidates, firstly because they can be effective at a low concentration (typically micro- to millimolar). Indeed, surfactants have been shown to be very efficient to control or cancel the coffee-ring effect, either by creating interfacial energy gradients leading to Marangoni flows,[24] or by inducing particle adsorption at the drop water/air interface through a combination of electrostatic and hydrophobic effects.[9,25,26] It is generally believed that a more hydrophobic surfactant is more efficient, *i.e.*, a lower concentration is needed, to affect or cancel the coffee- ring effect because it has stronger surface activity and its cooperative assembly on oppositely charged particles is favored. But what would happen for a surfactant of given chain length but higher electrostatic charge, which would result in a lower hydrophobicity but higher electrostatic interaction? This open question has yet to be solved if one wants to understand how charged surfactants determine the patterns of particle deposits from drying suspension drops. Secondly, some surfactants can be stimulus-responsive, thus offering the advantageous possibility to dynamically tune their properties in a user-controlled fashion. This was for instance successfully applied with photosensitive surfactants[27,28] to efficiently photocontrol the CRE[25] as well as to direct particle assembly on surfaces[12,13] using an external light stimulus. Such an approach offered excellent and remote spatio-temporal control of particle

deposition from drying drops but required the implementation of azobenzene-containing molecules as well as resilient to UV irradiation. Surprisingly, no other types of stimulus-responsive surfactants have been explored as possible alternative to photosensitive ones, and controlling the CRE has thus been mainly limited to more conventional formulation approaches. To address the two-fold challenge of rationalizing the roles of surfactant amphiphilicity and electrostatics in the CRE and exploring a totally new way of controlling it, we studied for the first time the deposition pattern from aqueous sessile drops containing particles and a surfactant with a charge and amphiphilic character that depend on its reduction-oxidation (redox) state. Redox-sensitive surfactants have been investigated for various applications, such as stimulus-responsive micelles and emulsions[29–33], DNA compaction[34] or interfacial flow control[35–37], but have never been reported for directing the deposition of particles in general nor controlling the CRE in particular. In this work, we synthesized and characterized redox-sensitive cationic surfactants of different chain lengths prior to analyzing the patterns obtained from evaporating drops containing anionic particles and the synthesized surfactants at different concentrations and redox states. This allowed us to efficiently control the drop deposition patterns, including the full cancelation of the CRE, with a redox stimulus for the first time. At a fundamental level, this study also contributed to disentangle the respective roles electrostatics and amphiphilicity in surfactant-based control of particle deposition from drying drops.

Materials and methods

Materials. Milli-Q water (Millipore, 18.2 MΩ·cm) was used for all experiments. A suspension of negatively charged Polystyrene particles (diameter 1 μm, concentration 4 wt. %) bearing a high density of carboxyl functional groups on their surface was purchased from Life Technologies (CML latex, catalogue number C37255) and used as received. Prior to each

experiment, the particle suspension was mixed vortexing (1 min), sonicated in an ultrasound bath (1 min) and vortexed again (30 s). Lithium sulfate monohydrate (CAS 10102-25-7, Merck, purity > 99 %), iron (III) sulfate (CAS 15244-10-7, Merck, purity > 97 %), iron (II) sulfate heptahydrate (CAS 7782-63-0, Merck, purity > 99 %), trimethylamine solution (CAS 75-50-3,4.2 M in ethanol), (6-bromohexyl)-ferrocene (CAS 136237-36-0, Merck), 11-bromoundecanoic acid (CAS 2834-05-1, Merck, purity > 99 %), thionyl chloride (CAS 7719-09-7, Merck, purity > 99 %), N,N-dimethylformamide (DMF, CAS 68-12-2, Merck, purity > 99%), aluminum chloride (CAS 7446-70-0, Merck, purity > 99 %), ferrocene (CAS 102-54-5, Merck, purity > 98 %), sodium borohydride (CAS 16940-66-2, Merck, purity > 98 %), toluene (CAS 108-88-3, Carlo Erba, purity > 95 %), dichloroethane (DCE, CAS 107-06-2, Carlo Erba, purity > 95 %), dichloromethane (DCM, CAS 75-09-2, Carlo Erba, purity > 95 %), ethanol (CAS 64-17-5, Merck, purity > 98 %), heptane (CAS 142-82-5, Carlo Erba, purity > 95 %), petroleum ether 30-40 °C (PE, CAS 64742-49-0, Carlo Erba, purity > 95 %) and tert-butylmethyl ether (TBME, CAS 1634-04-4, Carlo Erba, purity > 95 %) were all used without purification. Tetrahydrofuran (THF, CAS 109-99-9 Carlo Erba, purity > 98 %) was freshly distilled from a mixture with solid sodium before use.

F_6TAB$^+$ synthesis. (6-ferrocenylhexyl) trimethyl ammonium bromide (F_6TAB^+) was synthetized following procedure from Saji *et al.*[31] (see Fig. 2A). In a 25 mL round bottom flask, 1.8 mmol of (6-bromohexyl)-ferrocene **(1)** was introduced. An excess of 3.4 mL trimethylamine in 4.2 M solution in ethanol was added. Then, 3 ml of pure ethanol was added and the mixture was stirred for 5 days at room temperature. The mixture was evaporated under vacuum at 40 °C to remove ethanol to get a yellow oil. A yellow solid crystallized by addition of 3 ml of hexane. The solid was washed in 3 x 500 µL of hexane and dried under vacuum. Recrystallisation in a mixture 1:1 acetone: hexane gave 617 mg of pure F_6TAB^+ **(2)** as yellow solid (yield 85.5 %°), ^{1}H NMR (MeOD-D4) δ 4.0-4.1 (m, 9 H, ferrocene), 3.3 (m, 2 H, -C**H**$_2$-N$^+$(CH$_3$)$_3$), 3.1 (s, 9 H, - N$^+$(C**H**$_3$)$_3$), 2.4 (t, 2 H, ferrocene-C**H**$_2$-),

1.8 (q, 2 H, -C**H**$_2$-CH$_2$N$^+$(CH$_3$)$_3$), 1.3-1.6 (m, 16 H, - CH$_2$-C**H**$_2$-C**H**$_2$-). IR data agreed with product structure. The solid was permanently kept under Argon. By dilution in pure water, it gives a pure reduced F$_6$TAB$^+$ solution that slowly oxidize in time. The solubility of F$_6$TAB$^+$ was determined to be around 30 mM.

F$_{11}$TAB$^+$ synthesis. Step 1. (11-ferrocenylundecyl) trimethyl ammonium bromide (F$_{11}$TAB$^+$) was synthetized following the original procedure from Saji *et al.*[31] but with improvements (see Fig. 3A). For the first step, the procedure was improved from Garcìa-Barrantes *et al.*[38]. In a 200 mL round-bottom flask under argon and linked to a gas oil bubbler, 24.6 g of 11-bromoundecanoic acid **(3)** was mixed with 20 mL thionyl chloride (1 eq.) in 110 mL of anhydrous toluene. Some drops of DMF were added and the mixture was stirred for 3 hours at 40 °C. The reaction was followed using thin layer chromatography (solvent toluene). The mixture was evaporated under reduced pressure, 20 mL of toluene was added under argon and the mixture was evaporated again. The process was repeated two times. Acyl chloride **(4)** was obtained as a slightly yellow residue and identified with ^{1}H-NMR (CDCl$_3$) δ 1.3-2.3 (m, 16 H, Br-CH$_2$-(C**H**$_2$)$_8$-CH$_2$-COCl), δ 2.9 (t, 2 H, -C**H**$_2$-COCl) and δ 3.4 (t, 2 H, -C**H**$_2$-Br). Yield was 86 %.

Step 2. 20.4 g of acyl chloride **(4)** was dissolved in 100 mL anhydrous dichloromethane and 10.1 g of aluminum chloride (1 eq.) was added. In another round-bottom flask under argon, 14.7 g of ferrocene (1 eq.) was dissolved in 150 mL of anhydrous dichloromethane. Acyl chloride mixture was then added dropwise to the ferrocene mixture for around 30 minutes at 0 °C. The resulting solution was stirred for 1 hour at 0 °C and followed by thin layer chromatography (solvent toluene). When all acyl chloride has disappeared, around 100 mL HCl 2 M was added gently until the solution stopped to degas. Organic and aqueous phases were separated. The aqueous phase was extracted with three fractions of 20 mL of tert-butyl methyl ether. Organic phases were dried with magnesium sulfate and evaporated under reduced pressure. Product **(5)** was purified by a column chromatography (silica, PE, then TMBE and DE) and was identified with ^{1}H-NMR (CDCl$_3$) δ 1.2-1.5 (m, 10 H, Br-CH$_2$-CH$_2$-(C**H**$_2$)$_5$-), δ 1.7 (m, 2 H, Br-CH$_2$-CH$_2$-(CH$_2$)$_5$-C**H**$_2$-), δ 1.8-1.9 (m, 2 H, Br-CH$_2$-C**H**$_2$-(CH$_2$)$_5$-), δ

2.7 (t, 2 H, Fc-CO- C**H**$_2$-), δ 3.4 (t, 2 H, Br-C**H**$_2$-) and δ 4.2-4.8 (3*s, 9 H, **Fc**-). Yield was 83 %.

Step 3. This step was slightly improved from Li *et al.* procedure[39]. In a 1 L round-bottom flask under argon and equipped with a gas oil bubbler, 26.2 g of ferrocene carbonyl product **(5)** was dissolved in 66 mL of dry tetrahydrofuran. In a 500 mL round bottom flask under argon, 9.4 g of sodium borohydride (4 eq.) and 16.3 g of aluminum chloride (2 eq.) were dissolved in 70 mL of dried tetrahydrofuran. Then, the ferrocene carbonyl mixture was added dropwise during around one hour at 0 °C with strong magnetic stirring under argon. The reaction was followed with thin layer chromatography (solvent PE:DE 20:1). Then, 105 mL of water was added dropwise to the mixture at 0 °C with strong stirring. Warning: the reaction is highly exothermic. Once the mixture became less reactive,150 mL of HCl at 1 M was added. Phases were separated and the aqueous phase was extracted with three 20 mL fractions of PE. Organic phases were dried with magnesium sulfate and evaporated under reduced pressure. A crude orange-yellow oil was obtained. Product **(6)** was recrystallized in PE and filtrated through silica frittered glass and finally identified with $_1$H-NMR ($CDCl_3$) δ 1.2-1.6 (m, 12 H, Br-CH_2-CH_2-(C**H**$_2$)$_6$-), δ 1.8-1.9 (q,2 H, Br-CH_2-C**H**$_2$-$(CH_2)_5$-), δ 2.3 (t, 2 H, Fc-C**H**$_2$-), δ 3.4 (t, 2 H, Br-C**H**$_2$-) and δ 4.1 (s, 9 H, **Fc**-). Yield was 70 %.

Step 4. 17.7 g of alkyl bromide **(6)** was mixed with 100 mL of trimethylamine solution in ethanol (8 eq.) and 100 mL of THF. The mixture was stirred under reflux at 40 °C for one day.Then, it was evaporated under vacuum. Product **(7)** recrystallized after mixing vigorously in TBME. It was filtrated, dried overnight on a Schlenk line and identified with $_1$H-NMR (MeOD- 4D) δ 1.3-1.6 (m, 8 H, Br$(CH_3)_3$N-CH_2-CH_2-(C**H**$_2$)$_8$-), δ 1.8 (q, 2 H, Br$(CH_3)_3$N-CH_2-C**H**$_2$-), δ 2.32 (t, 2 H, Fc-C**H**$_2$-), δ 3.1 (s, 9 H, Br(C**H**$_3$)$_3$N-), δ 3.33 (t, 2 H, Br(C**H**$_3$)$_3$N-C**H**$_2$-) and δ 4.1 (s,9 H, **Fc**-). Yield was 99 % and synthesis overall yield was 49 %.

Electrochemical properties. The electrochemical cell used was a 50 mL triple neck flat bottom flask filled with a day-made 30 mL solution of 1 mM F_6TAB with 100 mM Li_2SO_4 as electrolyte. The electrodes were a platinum disk (50 μm diameter) as the working electrode, a platinum wire (1

mm diameter) as the counter electrode and a silver reference electrode (REF) covered with silver oxide. All electrochemical experiments were performed at room temperature using a potentiostat PGSTAT 30 controlled by GPES4.9 software. Cyclic voltammetry was carried out between -0.25V and 0.4V at 10 $mV \cdot s^{-1}$ scan rate, without stirring (Figure 2B). The same procedure was used for 2 mM $F_{11}TAB$ (Figure 3B).

Electrochemical oxidation. Experiments were performed at a constant potential using the same electrochemical cell with a strong magnetic stirring. A platinum grid with a high surface area ~3 cm^2 was used as the working electrode. The counter electrode was inserted in a separated compartment filled with 100 mM Li_2SO_4 electrolyte. The F_6TAB solutions were oxidized to F_6TAB^{2+} at E = +0.25V or reduced to F_6TAB^{+} at E = -0.25V during 3600 s.

UV-visible absorbance and absorption coefficients. Absorbance spectra were obtained with Bio Spectrophotometer (Eppendorf). For F_nTAB solutions at various oxidation rates in pure water, water was used as a reference. For F_nTAB solution containing electrolyte Li_2SO_4 at 100 mM, a solution of 100 mM Li_2SO_4 was used as reference. Measurements were performed in 1 cm wide plastic cuvette. Molar absorbance coefficient of F_6TAB^{+} (reduced), F_6TAB^{2+}(oxidized), $F_{11}TAB^{+}$ (reduced) and $F_{11}TAB^{2+}$ (oxidized) at 437 nm and 627 nm were deduced from absorbance spectra of solutions of F_nTAB (5 mM for n = 6; 2 mM for n = 11) in 100 mM Li_2SO_4 and at a defined oxidation rate controlled by chronoamperometry (Fig. S2).

Chemical oxidation. Six mother solutions of 2 mM F_nTAB were prepared in pure water. Each of them had a different oxidation rate {0; 0.20; 0.40; 0.60; 0.80; 1} obtained by addition of equivalent quantity of iron (III) ion from $Fe_2(SO_4)_3$. The iron (III) reacted fast and totally with F_nTAB^{+} to give iron (II) and F_nTAB^{2+} (Fig. S3). A series of control solutions was made without F_nTAB and with water and iron (III) at the corresponding concentrations.

Sample preparation and drop deposition. Mother F_nTAB solutions (2 mM), oxidized if necessary, as described above, were diluted in water and mixed with particle suspension to get the desired F_nTAB concentration and a final particle concentration of 4 $mg \cdot mL^{-1}$. All drops have been deposited in a volume of 1 µL (Eppendorf micropipette) on rectangular glass coverslips (24x 60 mm, Menzel-Gläser) for all experiments except for scanning electron microscopy (SEM) where circular glass coverslips (Menzel-Gläser, 1.5 cm in diameter) were used. Drop evaporation was achieved at 21 ± 2 °C and 45 ± 10 % relative humidity under a box to avoid air flow and dust contamination during drying.

Drops and deposits observation. All the samples have been observed using an inverted epifluorescence microscope (Observer D1, Zeiss) equipped with a sCMOS camera (Zyla 4.2 Plus, Andor Technology). For acquisition of whole deposits, a 4× magnification objective was used (UPlanFLN 4x, Olympus). For scanning electron microscopy (SEM) imaging, a gold layer was first deposited on the samples (sputtering system, 125 mA, 60 s) and then imaged at an incident angle of 90° with a tabletop SEM microscope (Hitachi, TM3030) at magnification ranging from 30× to 1000×.

Tensiometry. Interfacial energy has been recorded using a drop shape analyzer (DSA 30, Krüss). A 4 µL drop of desired concentration of F_nTAB and/or iron (III) from $Fe_2(SO_4)_3$ was generated at room temperature (21 ± 4 °C and 45 ± 20 % relative humidity). The drop shape was analyzed using the instrument software (DSA4, Krüss) to extract the water/air interfacial energy(Γ). The drop was protected from air flows and we waited about 10 min to reach stabilization and measure the equilibrium value of Γ.

Zeta potential. Zeta potential measurements have been conducted on Zetasizer Nano-ZS (Malvern Instruments). F_nTAB was diluted at desired concentration with iron (III) from $Fe_2(SO_4)_3$ and mixed with latex colloids. Because the concentration used in CRE experiments was too high to get reliable measurements, we used a final concentration was 0.4 $mg \cdot mL^{-1}$, which was ten times less than in CRE experiments. Final solution was agitated 30 s before measurement. The volume of sample was 850µL. Experiments were conducted at room temperature (25±1°C). Each zeta potential measurement was a mean from 10 to 50 individual measurements. This was repeated three times for each condition and averaged to give the zeta potential values plotted in Fig. S5.

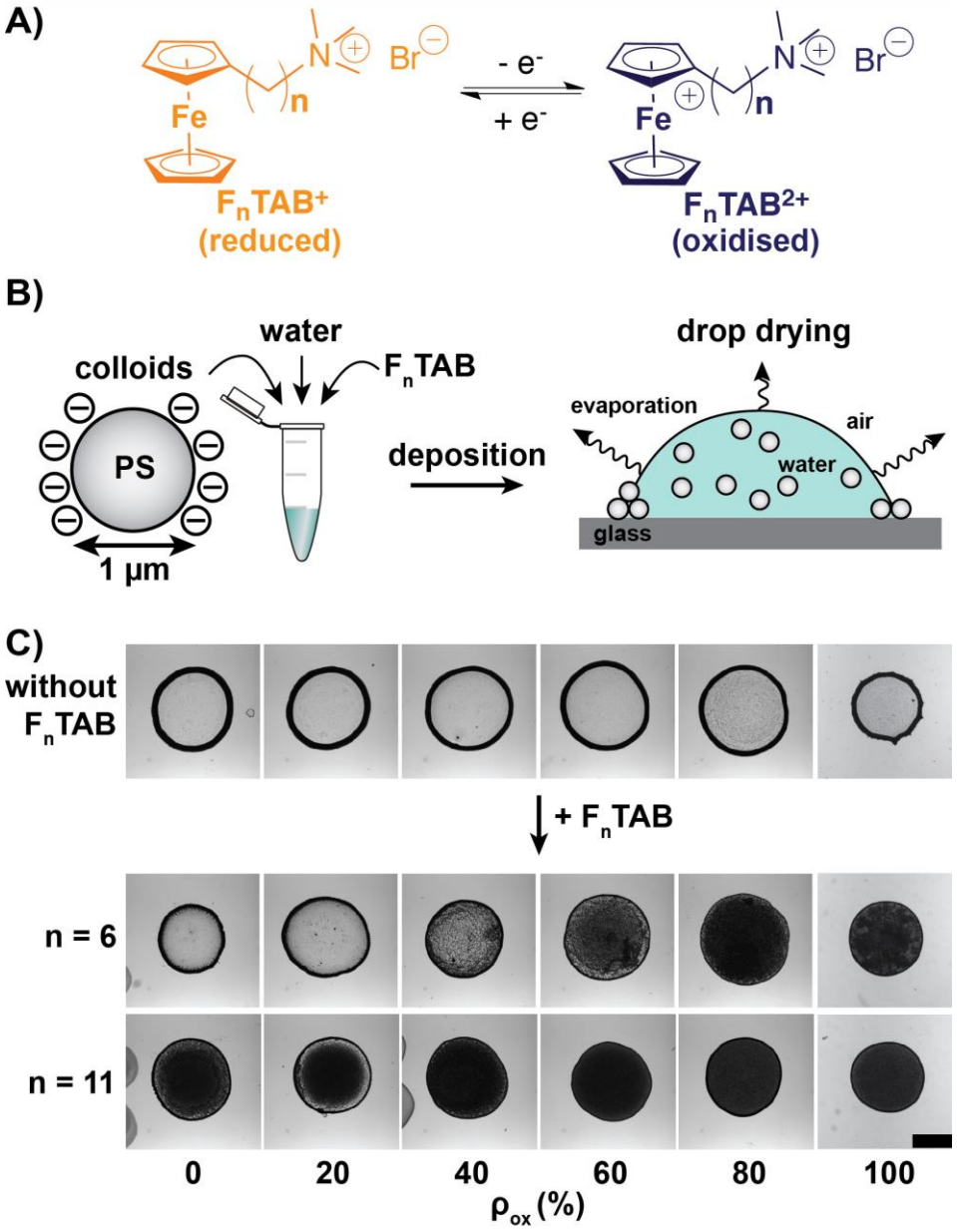

Figure 1. Redox control of the coffee-ring effect. *A) Reduced and oxidized forms of (n- ferrocenyln-alkyl)trimethyl ammonium bromide (F_nTAB) redox-sensitive surfactant. B) Scheme of the set-up for particle deposition: evaporation in air of a 1 µL sessile drop on glass containing anionic polystyrene particles (1 µm diameter, 4 mg·mL^{-1}) and F_nTAB. C) Representative transmission microscopy images of the deposits obtained in the absence of F_nTAB (top), with addition of 80 µM of F_6TAB (middle) or $F_{11}TAB$ (bottom) at oxidation rates (ρ_{ox} = [F_nTAB^{2+}]/[F_nTAB]) varying from 0% (pure F_nTAB^{+}) to 100% (pure F_nTAB^{2+}). Actual values of $_{ox}$ are given in Table S1. The scale bar is 1 mm.*

Results and Discussion

Figure 1 depicts our experimental system and shows the main result. We used two redox- sensitive surfactants, (6-ferrocenylhexyl)trimethyl ammonium bromide and (11- ferrocenylundecyl)trimethyl ammonium bromide surfactants referred to as F_nTAB with *n* equals 6 and 11, respectively. The reduced form, referred to as F_nTAB^+, has a neutral ferrocenyl group at the extremity of its hydrophobic tail and a quaternary ammonium bromide polar head (Fig. 1A, left). The oxidation of the ferrocenyl group leads to the oxidized form of F_nTAB, referred to as F_nTAB^{2+}, which contains an additional positive charge on its tail (Fig. 1A, right). To evaluate how a redox state can affect the CRE, a colloidal suspension containing anionic particles at a fixed concentration was supplemented with F_nTAB at different oxidation rates and concentrations (Fig. 1B, left). A drop (1 µL) of this mixture was deposited on a glass substrate and allowed to evaporate under room conditions (21 ± 2 °C and 45 ± 10% relative humidity) and protected from air flows (Fig. 1B, right). Under these conditions, full evaporation of the drop was achieved in about 30 to 40 min. In the absence of F_nTAB, all resulting particle deposits displayed a characteristic ring shape due to the evaporation-driven transport of particles toward the pinned contact line (Fig. 1C, top), in agreement with a conventional and strong CRE.[1,4] In contrast, the addition of F_nTAB led to a dramatic effect on the morphology of the dry deposit. For instance, with 80 µM of F_6TAB, the deposition pattern evolved from a ring to a disk shape when fraction of the oxidized form of the surfactant increased from 0% (fully reduced form, F_6TAB^+ only) to 100% (fully oxidized form, F_6TAB^{2+} only) (Fig. 1C, middle). This was also dependent on the amphilic character of the surfactant as, for the same surfactant concentration, only disks were obtained with the more hydrophobic $F_{11}TAB$ (Fig. 1C, bottom). To our knowledge this is the first time that the CRE is controlled through a redox stimulation and the detailed analysis of this new principle, and the effects of the parameters that control it, are described in the following.

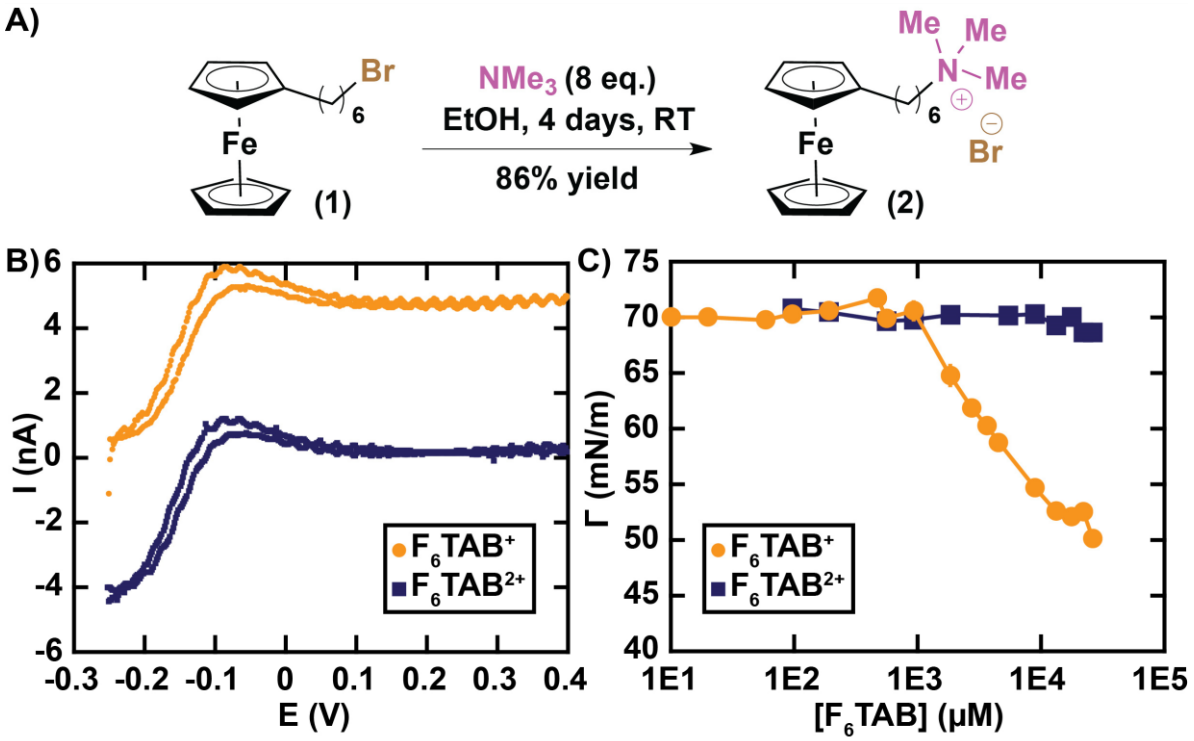

Figure 2. Synthesis and properties of F_6TAB. *A) Synthesis scheme. B) Steady-state voltamogramms (current vs potential) of the reduced (F_6TAB^+, orange disks) and oxidized (F_6TAB^{2+}, blue squares) forms of F_6TAB (5 mM) in an aqueous solution of Li_2SO_4 (100 mM). C) Interfacial energy in air (Γ) of water containing F_6TAB^+ or F_6TAB^{2+}, as a function of surfactant concentration.*

F_6TAB, a short-tail redox-sensitive surfactant. Several F_nTAB surfactants have been described in literature but, in most cases with $n \geq 8$.[31] We first synthesized a shorter-chain F_nTAB surfactant with $n = 6$, which, to our knowledge, was mentioned in only two reports[40,41] devoted to the electroactivity of F_6TAB-tethered clay where the surfactant was obtained with a multistep synthesis and its interfacial properties were not documented. In our case, F_6TAB was obtained in a single step by a Hofmann alkylation of the bromide precursor (Fig. 2A, full protocol in SI). Cyclic voltammetry of F_6TAB showed a reversible redox behavior with an apparent standard potential of -0.15 V / REF (Fig. 2B). The oxidized state F_6TAB^{2+} and reduced state F_6TAB^+ were quantitatively generated by bulk electrolysis at the constant potentials E = +0.25 V and E = -0.25 V, respectively. Interestingly, the effect of F_nTAB on the interfacial energy of the water/air interface (Γ) depended on its redox

state. The reduced form, with its short neutral and hydrophobic tail, had no effect on Γ for [F_6TAB^+] < 1 mM, with an interfacial energy closed to that of pure water (70.8 ± 0.2 $mN \cdot m^{-1}$ under our experimental conditions), but significantly reduced Γ at higher concentrations (Fig. 2C). Γ continuously decreased when [F_6TAB^+] increased from 1 mM to 30 mM, due to increasing amounts of F-$_6TAB^+$ adsorbing at the water/air interface. Above 30 mM, solubility issues were observed and the critical micelle concentration (CMC) could thus not be reached in this system. In contrast, with the oxidized form, Γ remained constant and close to the value for water, with or without the amount of added iron (III) used for F_6TAB oxidation (Fig. S1), for the whole range of tested F_6TAB^{2+} concentrations (from 10 µM to 30 mM, Fig. 2C). This is explained by the additional charge at the extremity of the tail strongly reducing the amphiphilic character of F_6TAB^{2+} and therefore its propensity to adsorb at the water/air interface and affect the interfacial energy.

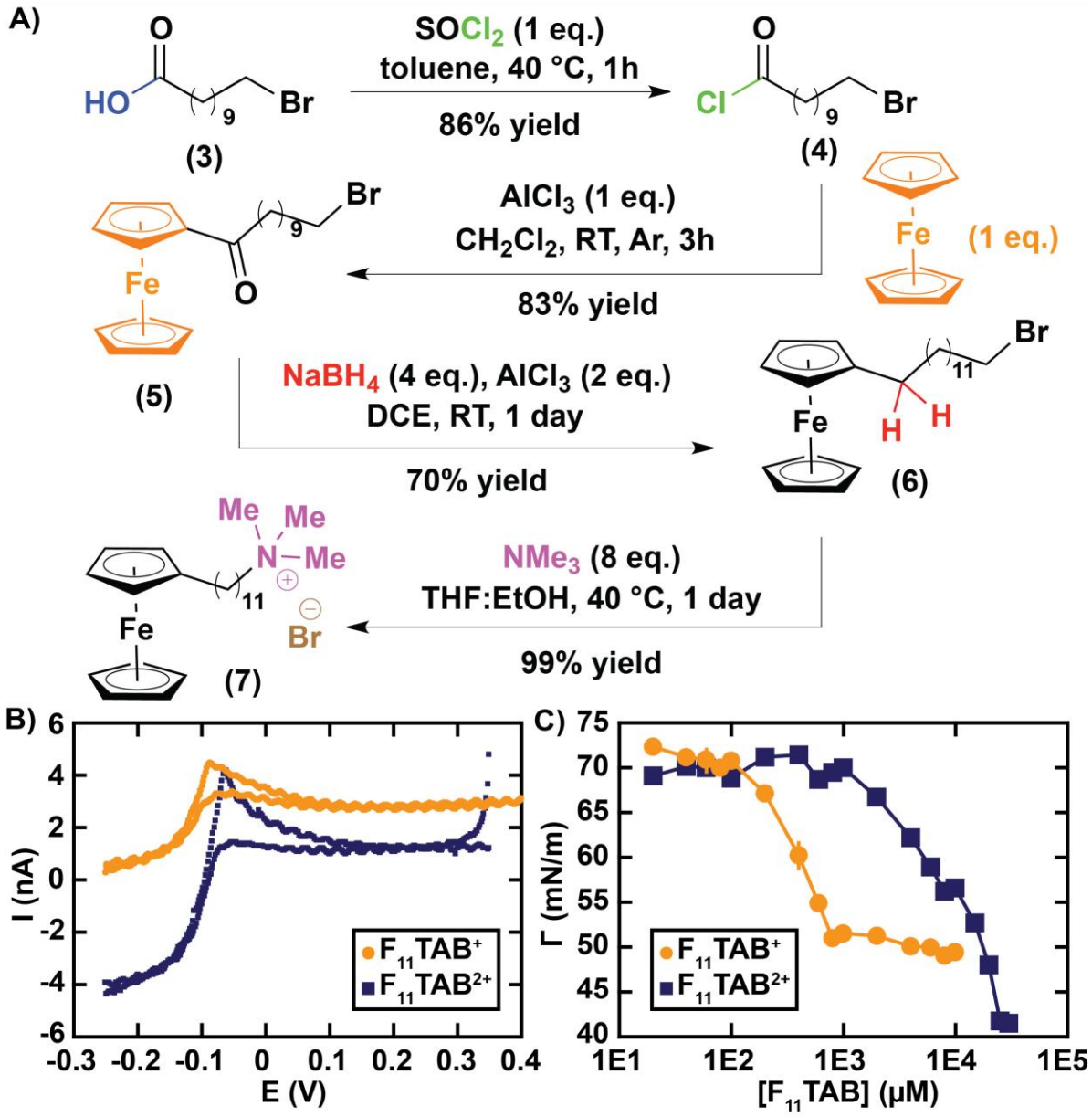

Figure 3. Synthesis and properties of $F_{11}TAB$. *A) Synthesis scheme. B) Steady-state voltamogramms (current vs potential) of the reduced ($F_{11}TAB^{+}$, orange disks) and oxidized ($F_{11}AB^{2+}$, blue squares) forms of $F_{11}TAB$ (2 mM) in an aqueous solution of Li_2SO_4 (100 mM). C) Interfacial energy in air (Γ) of water containing $F_{11}TAB^{2+}$ or F_6TAB^{2+}, as a function of surfactant concentration.*

F_{11}TAB, a redox-sensitive surfactant of higher hydrophobicity. To explore the behavior of a redox-sensitive surfactant with higher amphiphilic character, we synthesized F_{11}TAB, an analog of F_6TAB with 5 additional carbon atoms in the alkyl chain. The synthesis was improved from the original method by Saji *et al.*,[42] by optimizing conditions for better yield and replacing the methylated mercury-based conversion of **(5)** to **(6)** with a safer reaction combining carbonyl activation by Lewis acid and reduction by $NaBH_4$ (Fig. 3A, full protocol in SI). Cyclic voltammetry revealed a behavior similar to that of F_6TAB with identical reductive and oxidative potentials mainly controlled by the redox state of the ferrocene group (Fig. 3B). The reduced form of F_{11}TAB had a classical surfactant behavior affecting the water/air interfacial energy in a way similar to F_6TAB but with detectable effects starting at a much lower concentration (around 100 µM, Fig. 3C) due to the longer hydrophobic tail. In that case, the CMC was reached at around 800 µM, in agreement with previous reports.[43] Interestingly and contrary to its shorter- tail homolog, F_{11}TAB displayed interfacial effects even in its oxidized form, with Γ decreasing from 70 $mN \cdot m^{-1}$ to 41 $mN \cdot m^{-1}$ when [$F_{11}TAB^{2+}$] increased from 1 mM to 30 mM (Fig. 3C). With a longer carbon chain separating the two cationic charges at its extremities, $F_{11}TAB^{2+}$ can thus act as a bolaform surfactant capable of significantly reducing the water/air interfacial energy.

Redox control of deposition patterns. Using the set-up of Fig. 1B, we then systematically investigated the morphology of particle patterns deposited from evaporating sessile drops containing anionic particles and F_6TAB or F_{11}TAB at various concentrations and oxidation states. F_nTAB, initially synthesized in its reduced form, was oxidized by adding controlled amounts of iron (III). Absorbance spectroscopy (Fig. S2) of F_nTAB^+ (λ_{max} = 437 nm) and F_nTAB^{2+} (λ_{max} = 627 nm) allowed us to extract their molar extinction coefficients (Table S2) and quantify the F_nTAB oxidation rate, defined as ρ_{ox} = [F_nTAB^{2+}]/[F_nTAB], as a function of added iron (III) (Fig. S3). We found that the reaction was fast and almost quantitative, for both n = 6 (Fig. S3A,C) and n = 11 (Fig. S3B,D). This allowed us to adjust ρ_{ox} at stable values, which we named for convenience 0%, 20%, 40%, 60%, 80% and 100% (exact values given in Table S1).

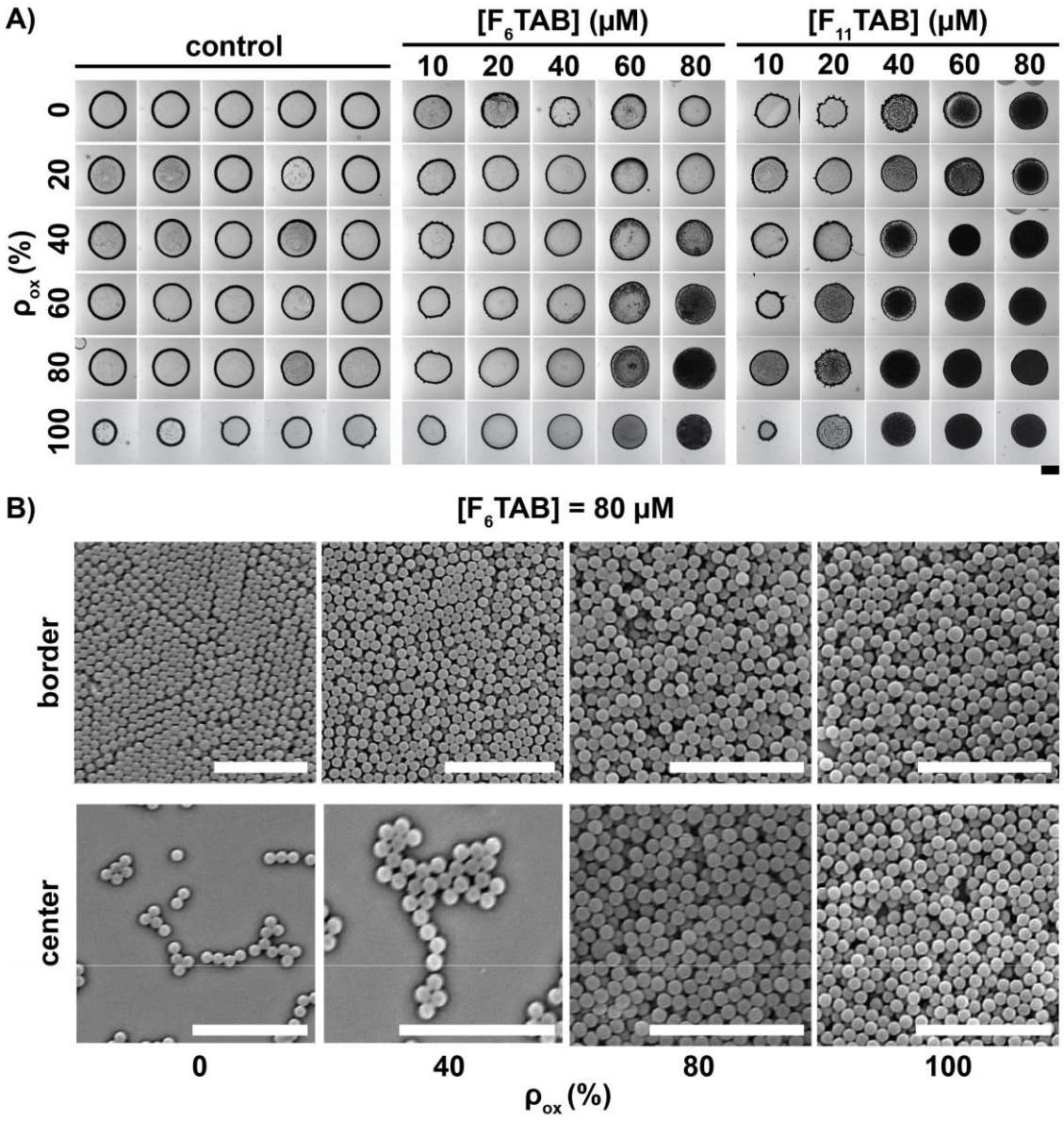

Figure 4. Redox control of the deposition patterns in the low surfactant concentration regime. *A) Representative transmission microscopy images of the deposition patterns obtained under conditions of Fig. 1B, with various concentrations (columns) and oxidation rates (lines) of F_nTAB with n = 6 (middle panel) and n = 11 (right panel). The left panel (control) shows the corresponding experiments without F_nTAB but in the presence of the amount of iron (III) used to control the oxidation rate (values in Fig. S4A). The scale bar is 1 mm. B) Representative scanning electron microscopy images taken in the border (top) or in the center (bottom) of deposited patterns with $[F_6TAB]$ = 80 μM at various oxidation rates. The scale bar is 10 μm.*

We started to explore the effect of adding F_nTAB at a low concentration (< 100 µM, Fig. 4A). Under these conditions, all patterns were highly reproducible with almost no depinning observed. In the absence of F_nTAB, and regardless of the amount of added iron (III) (Fig. S4), particles were transported by the evaporation-driven flow toward the pinned contact line where they accumulated to form typical ring-shaped deposition patterns (Fig. 4A, left). This confirms that CRE robustly occurred in our system and was not affected by the small amount of ions added to control the oxidation state. In contrast, adding F_nTAB to the suspension dramatically affected the deposition pattern (Fig. 4A, middle and right). With the reduced form of F_{11}TAB, we observed a progressive transition from a ring- to a disk-shaped pattern when [$F_{11}TAB^+$] increased from 0 to 80 µM (Fig. 4A, right). This can be explained by the progressive neutralization and hydrophobization of particles by surfactant adsorption, in agreement with zeta (ζ) potential evolution observed at lower particles and surfactants concentrations (Fig. S5), which led to particles adsorbing and accumulating at the water/interface instead of being transported by the evaporation-driven flow toward the contact line. Upon evaporation, adsorbed particles were eventually deposited by the descending interface to form a dense disk of particles, in agreement with the known mechanism of CRE cancellation by oppositely charged surfactants.[25,26] Interestingly, this evolution was observed for all oxidation rates tested but with the appearance of the disk morphology at a characteristic F_{11}TAB concentration significantly decreasing from about 80 µM to 40 µM when ρ_{ox} increased from 0 to 100 %, *i.e.*, when F_{11}TAB became both more charged and more hydrophilic (Fig. 4A, right). Since it is known that increasing the hydrophilicity of a surfactant decreases its efficiency to cancel the CRE[25,26] by cooperative adsorption on oppositely charged particles,[44] this result shows for the first time that the electrostatic neutralization of the particles by surfactant adsorption predominates hydrophobic effects to control the CRE. As a consequence, we could tune the morphology of the deposition pattern at a fixed F_{11}TAB concentration by simply adjusting the surfactant redox state. For instance, with [F_{11}TAB] = 20 µM, patterns evolved from a ring to a more homogeneous disk pattern when ρ_{ox} increased from 0 to 100 % (Fig. 4A, right). The same overall pattern evolution was observed with

F_6TAB (Fig. 4A., middle) but the transition from ring to disk was obtained either at higher oxidation rate for the same surfactant concentration, or at a higher surfactant concentration (80 µM) for the same oxidation evolution (Fig. 1C). This shows that for a given surfactant charge, increasing the hydrophobicity of its tail increases its efficiency to cancel the CRE by favoring its capability to neutralize oppositely charged particles through cooperative adsorption, an effect established for monovalent surfactants[25,26] but never observed for a higher nor varying electrostatic charge of the polar head. Using scanning electron microscopy (SEM), we finally analyzed the microscopic organization of particles in the deposits obtained with 80 µM F_6TAB (Fig. 4B) and with 20 µM $F_{11}TAB$ (Fig. S6). In both cases, with an increase in ρ_{ox}, we observed a progressive transition from heterogenous deposition (ring) of ordered particles (polycrystalline assemblies) to more uniform deposition (disk) of disordered particles. Due to the progressive neutralization of particles with the increase in surfactant charge, highly repulsive particles at low ρ_{ox} were transported to the contact line by the CRE and packed there in an ordered manner[45] while at high ρ_{ox} they became less repulsive (more "sticky") and accumulate at the water/air interface to be deposited in an amorphous manner.[26]

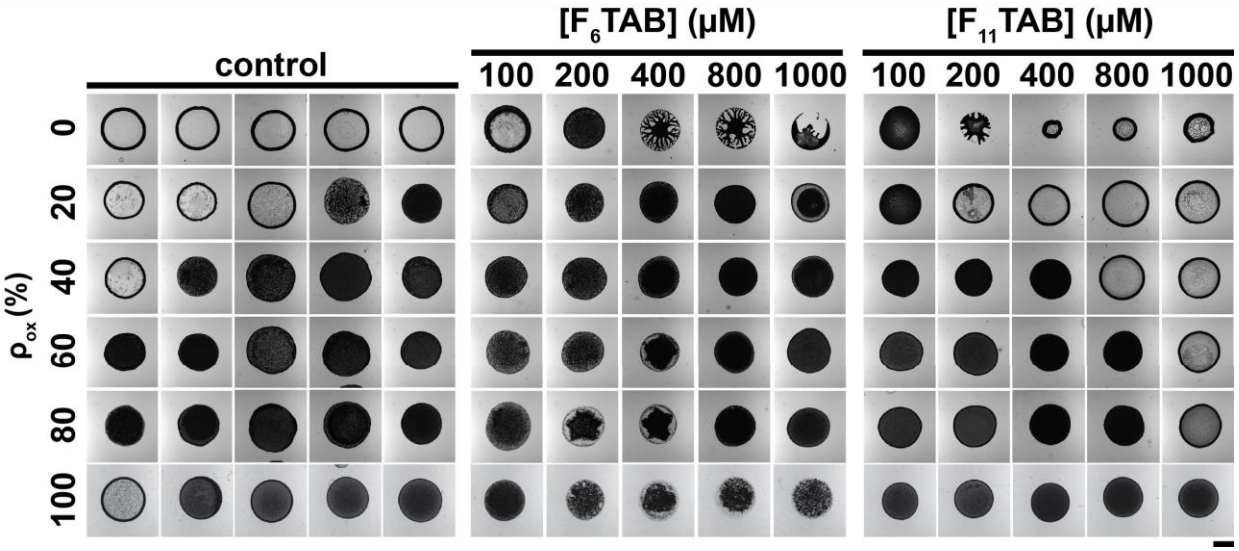

Figure 5. Redox control of the deposition patterns at high surfactant concentrations (≥ 100 µM). *Representative transmission microscopy images of the deposition patterns obtained under*

conditions of Fig. 1B, with various concentrations (columns) and oxidation rates (lines) of F_nTAB with n = 6 (middle panel) and n = 11 (right panel). The left panel (control) shows the corresponding experiments without F_nTAB but in the presence of the amount of iron (III) used to control the oxidation rate (values in Fig. S4B). The scale bar is 1 mm.

When F_nTAB was used at a higher concentration (100 – 1000 µM), a significantly different phenomenology was observed (Fig. 5). Without added oxidizing salt (ρ_{ox} = 0), even if fingering instabilities (e.g., [F_6TAB] = 400 µM or 800 µM) and/or contact line depinning (e.g., [$F_{11}TAB$] = 400 – 1000 µM) were observed, it appeared that increasing [F_nTAB] resulted in the maintenance of mainly disk-like deposits for n = 6 while ring-like patterns emerged for n = 11. $F_{11}TAB$ thus behaved as a conventional cationic surfactant, with overcharging of the particles at high concentration due to bi- to multilayered surfactant adsorption on the particle surface (Fig. S5), thus preventing particles to adsorb at the water/air interface and favoring the CRE again.[25,26] In contrast, F_6TAB^+, which has much weaker amphiphilic properties in this concentration range (Fig. 2C) than $F_{11}TAB^+$ (Fig. 3C), had much less propensity to self-assemble on particle surfaces to form bi- or multilayers resulting in the incapability to overcharge the particles (Fig. S5). For ρ_{ox} > 0, the increasing amount of multivalent salts used to control the oxidation state resulted in the formation of disk patterns in the absence of F_nTAB (Fig. 5, left). Notably, this phenomenon was correlated with iron (III) concentration, with rings and disks systematically occurring for iron (III) ≤ 60 µM and ≥ 150 µM, respectively (Fig. S7). By screening electrostatic interactions, multivalent cations at high concentration are known to induce the adsorption of anionic particles at the water/air interface,[46] thus preventing the CRE and allowing a homogenization of the particle deposits. With its low amphiphilic properties, F_6TAB did not perturb this effect and disks were systematically obtained (Fig 5, middle). In contrast, with its stronger amphiphilic character, $F_{11}TAB$ could counter-act the salt effect and induce the formation of rings at high concentration (Fig. 5, right), probably again by multilayered adsorption of $F_{11}TAB^+$ and particle overcharging. However, increasing ρ_{ox} was accompanied by an increasing relative amount of $F_{11}TAB^{2+}$ which has a much-reduced self-assembling character (Fig. 3C). As a consequence, rings could be obtained only when a sufficient remaining amount of $F_{11}TAB^+$ was present in solution ([$F_{11}TAB^+$] > 300 µM) as shown by the correlation between ring occurrence and remaining [$F_{11}TAB^+$] (Fig. S8). Hence, the total concentration of $F_{11}TAB$ necessary to obtain a ring pattern in this regime increased with ρ_{ox} (Fig. 5 right).

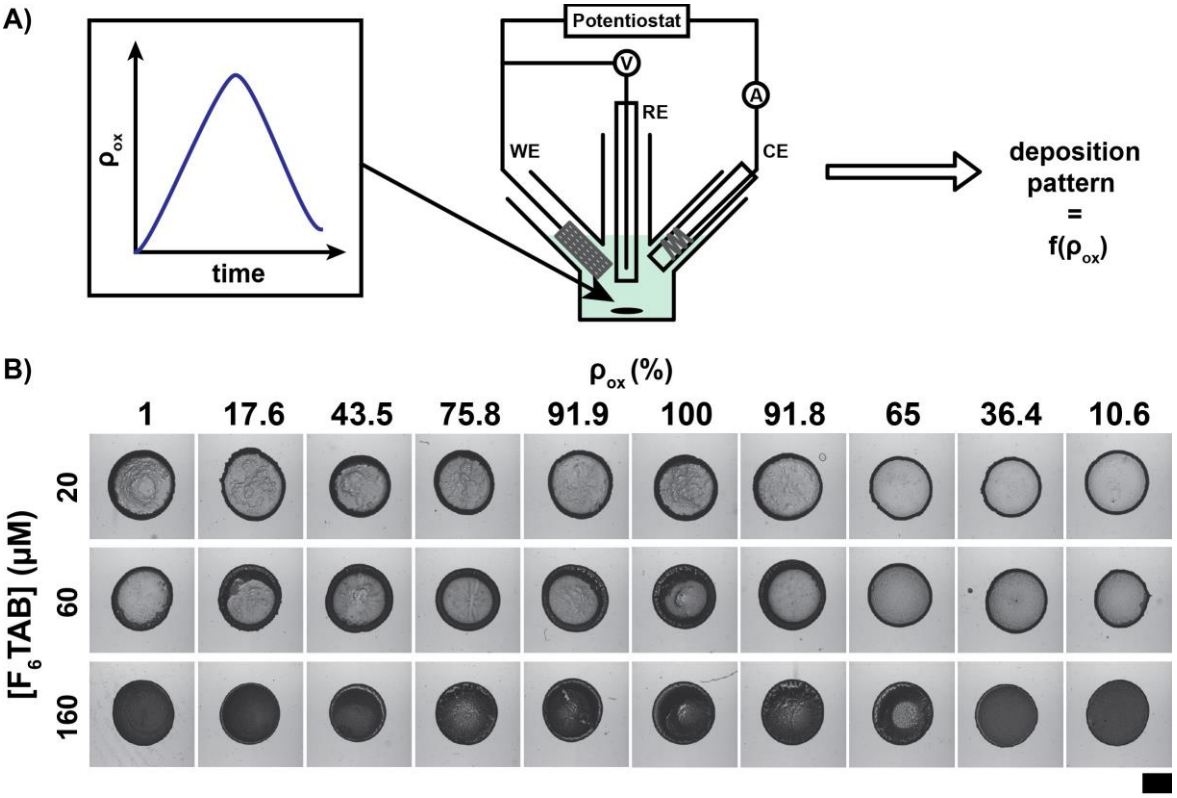

Figure 6. Electrochemical control of particle deposition in a closed system. *A) Scheme of the experiment. Without adding any chemical, applying a constant potential in a three-electrode redox cell containing F_6TAB allows us to dynamically adjust its oxidation rate as a function of time, which in turn allows us to control the particle pattern after drop deposition and drying. B) Representative transmission microscopy images of the deposition patterns as a function of the actual oxidation rate of F_6TAB for [F_6TAB] = 20 µM (top), 50 µM (middle) or 160 µM (bottom).*

Dynamic electrochemical control in a closed system. We demonstrated that the deposition pattern was controlled by adjusting the oxidation rate of the redox-sensitive surfactant F_nTAB obtained through addition of oxidizing entities (iron III ions). We thus explored whether it could be possible to achieve a similar redox control but in a closed system, *i.e.*, without adding any variable amounts of reducing or oxidizing molecules. To this end, we used a three-electrodes chronoamperometry set-up to adjust the oxidation rate of a F_6TAB solution (5 mM in a solution of 100 mM Li_2SO_4) in time, by applying an oxidation potential of +0,25 V +0.25 V followed by a reduction potential of -0.25 V (Fig. 6A). This resulted in increase of ρ_{ox} upon oxidation up to 100% followed by a decrease over

time when F_6TAB was *in situ* reduced again. Aliquots of that solution were taken along the course of the reaction and the actual value of ρ_{ox} was established by absorbance. Each of these samples was diluted to a desired concentration of F_6TAB, mixed with particles (2 mg·mL^{-1}) and a drop of the resulting suspension was allowed to dry under the conditions of Fig. 1B. We found that the pattern evolution upon F_6TAB electrochemical oxidation (Fig. 6B) was in striking agreement with what was observed by chemically oxidizing F_6TAB (Fig. 4A, middle). Regardless of ρ_{ox}, deposits displayed a ring-like morphology at a low F_6TAB concentration (20 µM) when the surfactant did not interact much with the oppositely charged particles (Fig. 6B, top) and a disk-like one at a higher concentration (160 µM) when the surfactant electrostatically adsorbed and neutralized the particles (Fig. 6B, bottom). Notably, at the same intermediate F_6TAB concentration (60 µM), a similar and progressive evolution from a ring-like pattern to a more homogenous disk was observed when ρ_{ox} first increased from almost 0 to 100 % (Fig. 6B, middle), interpreted as a signature of the increased electrostatic binding between F_6TAB and the particles upon enriching the solution in the oxidized, dicationic form of the surfactant. This consistent pattern evolution as a function of F_6TAB concentration and its oxidation rate, regardless of the nature of the oxidation method (electrochemical vs chemical) highlights the flexibility of the redox control approach as well as it highlights the determinant role of ρ_{ox} in directing the morphology of particle deposits. The electrochemical actuation also allowed us to reverse the stimulation by reducing F_6TAB once it was fully oxidized. We found that the resulting pattern evolution was fully reversible for all tested concentrations (Fig. 6B). This was particularly noticeable for the intermediate concentration ([F_6TAB] = 60 µM) for which the patterns evolved back from a disk-like shape to a marked ring pattern when ρ_{ox} decreased from 100% to 10.6%. Note that, in the absence of F_6TAB, only ring-shaped patterns were obtained (Fig. S9), showing that any significant role of remaining amounts of Li_2SO_4 after dilution can be excluded. All these results demonstrate that the redox control of particle deposition from drying drops is not limited to chemical oxidation and can be robustly controlled through an electrochemical approach, thus allowing dynamic and additive-free modulation of the deposited patterns.

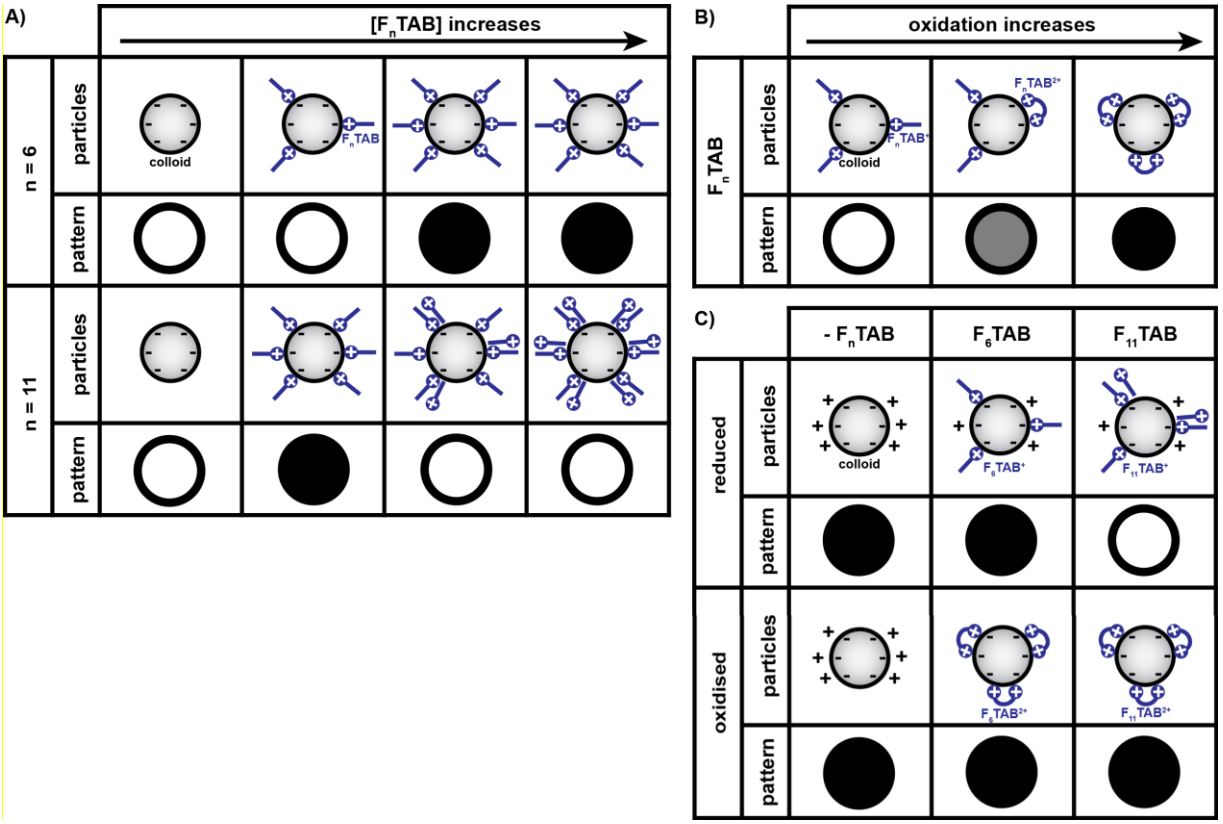

Figure 7. Schematic evolution of the colloid-surfactant interaction and resulting deposition pattern as a function of A) FnTAB concentration, B) oxidation rate andC) in the presence of high amounts of multivalent salts.

Overview. Figure 7 summarizes, in a schematic manner, the role of the main parameters we have investigated to control particle deposition in drying drops containing anionic colloids and cationic redox-sensitive surfactants. Without FnTAB, the evaporation-driven flow accumulated charged colloids at the contact line where repulsive particles assembled in an ordered fashion to form a polycrystalline ring. Increasing FnTAB concentration led to a neutralization of the particles and their accumulation at the water-air interface to form a uniform and amorphous disk- shaped deposit (Fig. 7A). This is similar to what can be obtained with conventional salts at millimolar concentrations except that this effect occurred here in a micromolar concentration regime due to the cooperative adsorption of surfactants on the oppositely charged surface of the anionic colloids. This self-

assembly is all the more efficient that surfactants are hydrophobic, explaining that, for a given oxidation rate, $F_{11}TAB$ led to the formation of disk at a lower concentration than F_6TAB (Fig. 7A). A further increase in $F_{11}TAB$ concentration led to formation of rings again due to the overcharging of the particles by multilayered adsorption of the surfactant on their surface, in agreement with the known effect of cationic surfactants on the CRE.[25,26] However, we observed for the first time that this was not the case for a short- hydrophobic tail surfactant such as F_6TAB because its reduced self-assembly ability prevented from efficient particle overcharging. Increasing hydrophobic effects, by favoring surfactant self- assembly and cooperative adsorption on oppositely charged nanoparticles, thus promoted both the formation of uniform disk patterns at low surfactant concentrations and reappearance of rings at higher concentrations. Interestingly, we found that oxidizing F_nTAB, although decreasing its hydrophobic and self-assembly character, led to a transition from a ring to disk pattern for both F_6TAB and $F_{11}TAB$ (Fig. 7B). This was due again to the neutralization of particles which, at a fixed F_nTAB concentration, was more efficient at a higher fraction of the dicationic form of the surfactant, *i.e.*, at a higher oxidation rate. This emphasizes the predominant role of electrostatics in controlling the CRE in oppositely charged particle-surfactant systems and how surfactant self- assembly can modulate it. Increasing surfactant chain length thus decreased the concentration at which the ring-to-disk transition was obtained either by adding surfactant of a given oxidation rate or by oxidizing a fixed concentration of the surfactant (Fig. 4A). Finally, studying high concentrations of surfactant involved high amounts of iron(III)/iron(II) and thus allowed to have insights on the effect of surfactants versus that of multivalent salts present in the solution (Fig.7C). At high salt concentrations, disk patterns were systematically obtained in the absence of surfactants. When surfactants were added, this was unchanged as long as surfactants were not hydrophobic enough to create multilayers and overcharge the particles. This was the case for F_6TAB^+ and F_6TAB^{2+} (too short tail) and $F_{11}TAB^{2+}$(too polar). Only sufficiently large amounts $F_{11}TAB^+$ (high $F_{11}TAB$ concentration and low oxidation rate) could over charge the particles and avoid their accumulation at the water-air interface, leading to ring-shaped patterns.

Conclusions

We showed for the first time how the deposition pattern from a drying sessile drop could be controlled by a redox stimulus, at both macroscopic (from ring to disk morphology) and microscopic (from crystalline to amorphous) levels. Achieved by simply adding a redox- sensitive surfactant in a colloidal suspension drop, the method allowed not only a full cancellation of the coffee-ring effect (CRE) but also a reproducible and user-defined adjustment of the deposit morphology, ranging from a marked ring to a homogenous disk pattern when typically switching from reductive to oxidizing conditions. We demonstrated that the oxidation rate of the surfactant can be tuned either chemically by simply adding oxidizing molecules or electrochemically through in situ application of a potential in an additive-free manner, highlighting the robustness, flexibility and reversible character of the approach. At a fundamental level, this study significantly improved our understanding of the general role of surfactants in controlling the CRE of oppositely charged colloids, with the following points that are worth being highlighted: 1) by promoting particle accumulation at the water/air interface, electrostatic screening and particle neutralization is the key-factor in the cancellation of the CRE; 2) increasing surfactant charge amplifies the phenomenon and overcomes hydrophobic effects; 3) the presence of the hydrophobic tail, by promoting self-assembly, makes surfactants behave i) as "super-salts" to neutralize particles and favor CRE cancellation at a very low concentration and ii) as "anti-salts" at high concentration by overcharging particles and inducing CRE again; 4) as a consequence, increasing surfactant hydrophobicity shifts the cancellation of the CRE to lower surfactant concentration while also favoring its reappearance by particle overcharging. Overall, this work brings new practical and fundamental solutions to cancel the CRE in many situations when it is deleterious or, on the contrary, to harness it to organize particles on surfaces in a controlled manner. By straightforward adjustment of the redox state, a fine tuning of the particle deposition can be done, from the overall distribution of particles on a surface to their microscopic organization. Conversely, this principle makes now possible to get information on the redox state of a sample liquid by simply

visualizing the deposition pattern left by a drying µL-sized drop, thus constituting a novel and advantageously simple concept for rapid and portable diagnostics with applications ranging from materials analysis to point-of-care biomedical monitoring.

ASSOCIATED CONTENT

Supporting Information. Supplementary figures S1-S8; supplementary tables S1-S2.

AUTHOR INFORMATION

Corresponding Author

* Email: damien.baigl@ens.psl.eu

Author Contributions

The manuscript was written through contributions of all authors. All authors have given approval to the final version of the manuscript.

Funding Sources

This work has received the support of "Institut Pierre-Gilles de Gennes" (laboratoire d'excellence), "Investissements d'avenir" program ANR-10-IDEX-0001-02 PSL, ANR-10- LABX-31, and ANR-10-EQPX-34.

Acknowledgment

We thank Yong Chen (Ecole Normale Supérieure) for providing us with the access to the scanning electron microscope. P.E.G. thanks M. Dagousset and N. Jamin for providing helpful teleworking conditions during SARS-CoV-2-related lockdown.

Competing interests

The authors declare no competing financial interest.

REFERENCES

(1) Deegan, R. D.; Bakajin, O.; Dupont, T. F.; Huber, G.; Nagel, S. R.; Witten, T. A. Capillary Flow as the Cause of Ring Stains from Dried Liquid Drops. *Nature* **1997**, *389* (6653), 827–829.

(2) Poulichet, V.; Morel, M.; Rudiuk, S.; Baigl, D. Liquid-Liquid Coffee-Ring Effect. *J. Colloid Interface Sci.* **2020**, *573*, 370–375.

(3) Larson, R. G. Re-Shaping the Coffee Ring. *Angew. Chemie - Int. Ed.* **2012**, *51*, 2546–2548.

(4) Larson, R. G. Transport and Deposition Patterns in Drying Sessile Droplets. *AIChE J.* **2014**, *60* (5), 1538–1571.

(5) Park, J.; Moon, J. Control of Colloidal Particle Deposit Patterns within Picoliter Droplets Ejected by Ink-Jet Printing. *Langmuir* **2006**, *22* (8), 3506–3513.

(6) Blossey, R.; Bosio, A. Contact Line Deposits on CDNA Microarrays: A "Twin-Spot Effect." *Langmuir* **2002**, *18*, 2952–2954.

(7) Dugas, V.; Broutin, J.; Souteyrand, E. Droplet Evaporation Study Applied to DNA Chip Manufacturing. *Langmuir* **2005**, *21* (20), 9130–9136.

(8) Deng, Y.; Zhu, X.-Y.; Kienlen, T.; Guo, A. Transport at the Air/Water Interface Is the Reason for Rings in Protein Microarrays. *J. Am. Chem. Soc.* **2006**, *128* (9), 2768–2769.

(9) Anyfantakis, M.; Baigl, D. Manipulating the Coffee-Ring Effect: Interactions at Work. *ChemPhysChem* **2015**, *16* (13), 2726–2734.

(10) Zhang, Z.; Zhang, X.; Xin, Z.; Deng, M.; Wen, Y.; Song, Y. Controlled Inkjetting of a Conductive Pattern of Silver Nanoparticles Based on the Coffee-Ring Effect. *Adv. Mater.* **2013**, *25*, 6714–6718.

(11) Kuang, M.; Wang, L.; Song, Y. Controllable Printing Droplets for High-Resolution Patterns. *Adv. Mater.* **2014**, *26* (40), 6950–6958.

(12) Varanakkottu, S. N.; Anyfantakis, M.; Morel, M.; Rudiuk, S.; Baigl, D. Light-Directed

Particle Patterning by Evaporative Optical Marangoni Assembly. *Nano Lett.* **2016**, *16* (1),644–650.

(13) Anyfantakis, M.; Varanakkottu, S. N.; Rudiuk, S.; Morel, M.; Baigl, D. Evaporative Optical Marangoni Assembly: Tailoring the Three-Dimensional Morphology of Individual Deposits of Nanoparticles from Sessile Drops. *ACS Appl. Mater. Interfaces* **2017**, *9* (42),37435–37445.

(14) Trantum, J. R.; Wright, D. W.; Haselton, F. R. Biomarker-Mediated Disruption of Coffee- Ring Formation as a Low Resource Diagnostic Indicator. *Langmuir* **2012**, *28* (4), 2187– 2193.

(15) Wen, J. T.; Ho, C. M.; Lillehoj, P. B. Coffee Ring Aptasensor for Rapid Protein Detection. *Langmuir* **2013**, *29* (26), 8440–8446.

(16) Gulka, C. P.; Swartz, J. D.; Trantum, J. R.; Davis, K. M.; Peak, C. M.; Denton, A. J.; Haselton, F. R.; Wright, D. W. Coffee Rings as Low-Resource Diagnostics: Detection of the Malaria Biomarker Plasmodium Falciparum Histidine-Rich Protein-II Using a Surface-Coupled Ring of Ni(II)NTA Gold-Plated Polystyrene Particles. *ACS Appl. Mater. Interfaces* **2014**, *6* (9), 6257–6263.

(17) Li, Y.; Zhao, Z.; Lam, M. L.; Liu, W.; Yeung, P. P.; Chieng, C.-C.; Chen, T.-H. Hybridization-Induced Suppression of Coffee Ring Effect for Nucleic Acid Detection. *Sensors Actuators B Chem.* **2015**, *206*, 56–64.

(18) Devineau, S.; Anyfantakis, M.; Marichal, L.; Kiger, L.; Morel, M.; Rudiuk, S.; Baigl, D. Protein Adsorption and Reorganization on Nanoparticles Probed by the Coffee-Ring Effect: Application to Single Point Mutation Detection. *J. Am. Chem. Soc.* **2016**, *138* (36), 11623–11632.

(19) Mampallil, D.; Eral, H. B.; van den Ende, D.; Mugele, F. Control of Evaporating Complex

Fluids through Electrowetting. *Soft Matter* **2012**, *8* (c), 10614–10617.

(20) Wray, A. W.; Papageorgiou, D. T.; Craster, R. V; Sefiane, K.; Matar, O. K. Electrostatic

Suppression of the “Coffee Stain Effect.” *Langmuir* **2014**, *30* (20), 5849–5858.

(21) Malinowski, R.; Volpe, G.; Parkin, I. P.; Volpe, G. Dynamic Control of Particle Deposition in Evaporating Droplets by an External Point Source of Vapor. *J. Phys. Chem. Lett.* **2018**, *9* (3), 659–664.

(22) Sáenz, P. J.; Wray, A. W.; Che, Z.; Matar, O. K.; Valluri, P.; Kim, J.; Sefiane, K. Dynamics and Universal Scaling Law in Geometrically-Controlled Sessile Drop Evaporation. *Nat. Commun.* **2017**, *8*, 1–9.

(23) Talbot, E. L.; Yang, L.; Berson, A.; Bain, C. D. Control of the Particle Distribution in Inkjet Printing through an Evaporation-Driven Sol–Gel Transition. *ACS Appl. Mater. Interfaces* **2014**, *6* (12), 9572–9583.

(24) Still, T.; Yunker, P. J.; Yodh, A. G. Surfactant-Induced Marangoni Eddies Alter the Coffee-Rings of Evaporating Colloidal Drops. *Langmuir* **2012**, *28* (11), 4984–4988.

(25) Anyfantakis, M.; Baigl, D. Dynamic Photocontrol of the Coffee-Ring Effect with optically Tunable Particle Stickiness. *Angew. Chemie Int. Ed.* **2014**, *53*, 14077–14081.

(26) Anyfantakis, M.; Geng, Z.; Morel, M.; Rudiuk, S.; Baigl, D. Modulation of the Coffee-Ring Effect in Particle/Surfactant Mixtures: The Importance of Particle–Interface Interactions. *Langmuir* **2015**, *31* (14), 4113–4120.

(27) Diguet, A.; Guillermic, R. M.; Magome, N.; Saint-Jalmes, A.; Chen, Y.; Yoshikawa, K.; Baigl, D. Photomanipulation of a Droplet by the Chromocapillary Effect. *Angew. Chemie- Int. Ed.* **2009**, *48* (49), 9281–9284.

(28) Vialetto, J.; Anyfantakis, M.; Rudiuk, S.; Morel, M.; Baigl, D. Photoswitchable Dissipative Two-Dimensional Colloidal Crystals. *Angew. Chemie Int. Ed.* **2019**, *58* (27),9145–9149.

(29) Saji, T.; Hoshino, K.; Aoyagui, S. Reversible Formation and Disruption of Micelles by Control of the Redox State of the Surfactant Tail Group. *J. Chem. Soc. Chem. Commun.* **1985**, No. 13, 865–866.

(30) Hoshino, K.; Saji, T. Electrochemical Formation of an Organic Thin Film by Disruption of Micelles. *J. Am. Chem. Soc.* **1987**, *109* (19), 5881–5883.

(31) Saji, T.; Hoshino, K.; Ishii, Y.; Goto, M. Formation of Organic Thin Films by Electrolysis of Surfactants with the Ferrocenyl Moiety. *J. Am. Chem. Soc.* **1991**, *113* (2), 450–456.

(32) Muñoz, S.; Gokel, G. W. Redox-Switched Vesicle Formation from Two Novel, Structurally Distinct Metalloamphiphiles. *J. Am. Chem. Soc.* **1993**, *115* (11), 4899–4900.

(33) Takahashi, Y.; Koizumi, N.; Kondo, Y. Demulsification of Redox-Active Emulsions by Chemical Oxidation. *Langmuir* **2016**, *32* (30), 7556–7563.

(34) Hays, M. E.; Jewell, C. M.; Lynn, D. M.; Abbott, N. L. Reversible Condensation of DNA Using a Redox-Active Surfactant. *Langmuir* **2007**, *23* (10), 5609–5614.

(35) Gallardo, B. S.; Hwa, M. J.; Abbott, N. L. In Situ and Reversible Control of the Surface Activity of Ferrocenyl Surfactants in Aqueous Solutions. *Langmuir* **1995**, *11* (11), 4209–4212

(36) Bennett, D. E.; Gallardo, B. S.; Abbott, N. L. Dispensing Surfactants from Electrodes: Marangoni Phenomenon at the Surface of Aqueous Solutions of (11-Ferrocenylundecyl)Trimethylammonium Bromide. *J. Am. Chem. Soc.* **1996**, *118* (27), 6499–6505.

(37) Bai, G.; Graham, M. D.; Abbott, N. L. Role of Desorption Kinetics in Determining Marangoni Flows Generated by Using Electrochemical Methods and Redox-Active Surfactants. *Langmuir* **2005**, *21* (6), 2235–2241.

(38) García-Barrantes, P. M.; Lamoureux, G. V.; Pérez, A. L.; García-Sánchez, R. N.; Martínez, A. R.; San Feliciano, A. Synthesis and Biological Evaluation of Novel Ferrocene-Naphthoquinones as Antiplasmodial Agents. *Eur. J. Med. Chem.* **2013**, *70*,548–557.

(39) Li, C.; Ren, B.; Zhang, Y.; Cheng, Z.; Liu, X.; Tong, Z. A Novel Ferroceneylazobenzene Self-Assembled Monolayer on an ITO Electrode: Photochemical and Electrochemical

Behaviors. *Langmuir* **2008**, *24* (22), 12911–12918.

(40) Swearingen, C.; Macha, S.; Fitch, A. Ferrocene Groups Tethered to Clay Surfaces. *J. Electrochem. Soc.* **2002**, *149* (4), E103.

(41) Swearingen, C.; Wu, J.; Stucki, J.; Fitch, A. Use of Ferrocenyl Surfactants of Varying Chain Lengths to Study Electron Transfer Reactions in Native Montmorillonite Clay. *Environ. Sci. Technol.* **2004**, *38* (21), 5598–5603.

(42) Saji, T.; Hoshino, K.; Aoyagui, S. Reversible Formation and Disruption of Micelles by Control of the Redox State of the Surfactant Tail Group. *J. Chem. Soc. Chem. Commun.* **1985**, *53* (13), 865.

(43) Gallardo, B. S.; Metcalfe, K. L.; Abbott, N. L. Ferrocenyl Surfactants at the Surface of Water: Principles for Active Control of Interfacial Properties. *Langmuir* **1996**, *12* (17), 4116–4124.

(44) Deleurence, R.; Parneix, C.; Monteux, C. Mixtures of Latex Particles and the Surfactant of Opposite Charge Used as Interface Stabilizers - Influence of Particle Contact Angle, Zeta Potential, Flocculation and Shear Energy. *Soft Matter* **2014**, *10* (36), 7088–7095.

(45) Marín, Á. G.; Gelderblom, H.; Lohse, D.; Snoeijer, J. H. Order-to-Disorder Transition in Ring-Shaped Colloidal Stains. *Phys. Rev. Lett.* **2011**, *107* (8), 085502.

(46) Abdel-Fattah, A. I.; El-Genk, M. S. Sorption of Hydrophobic, Negatively Charged Microspheres onto a Stagnant Air/Water Interface. *J. Colloid Interface Sci.* **1998**, *202* (2), 417–429.

Graphical table of contents